

## TEXTILES

# Radiative human body cooling by nanoporous polyethylene textile

Po-Chun Hsu,<sup>1</sup> Alex Y. Song,<sup>2</sup> Peter B. Catrysse,<sup>2</sup> Chong Liu,<sup>1</sup> Yucan Peng,<sup>1</sup> Jin Xie,<sup>1</sup> Shanhui Fan,<sup>2</sup> Yi Cui<sup>1,3\*</sup>

Thermal management through personal heating and cooling is a strategy by which to expand indoor temperature setpoint range for large energy saving. We show that nanoporous polyethylene (nanoPE) is transparent to mid-infrared human body radiation but opaque to visible light because of the pore size distribution (50 to 1000 nanometers). We processed the material to develop a textile that promotes effective radiative cooling while still having sufficient air permeability, water-wicking rate, and mechanical strength for wearability. We developed a device to simulate skin temperature that shows temperatures 2.7° and 2.0°C lower when covered with nanoPE cloth and with processed nanoPE cloth, respectively, than when covered with cotton. Our processed nanoPE is an effective and scalable textile for personal thermal management.

Energy consumption and climate change are two major issues for humans in the 21st century. The high consumption of energy directly leads to excessive greenhouse gas emissions, which severely disturbs the climate balance and causes global warming and extreme weather (1, 2). Consequently, numerous efforts are being made to develop renewable energy such as solar, wind, ocean, hydrogen, and carbon-neutral fuels (3–9). On the other hand, reducing current energy consumption and improving energy efficiency are equally important. In fact, improving energy efficiency, through the use of energy-efficient appliances or building designs, is the most cost-effective way to solve the energy issue, as compared with other energy sources in the United States (10).

Space heating and cooling are the dominant parts of residential and commercial energy consumption. They contribute to 12.3% of total U.S. energy consumption. Reducing the demand for indoor temperature regulation will have substantial impact on global energy use (11–13). Although conventional approaches have been focusing on improving building insulation and enabling smart temperature control (14–16), the concept of “personal thermal management” is emerging as a promising alternative. The objective of personal thermal management is to provide heating or cooling only to a human body and its local environment, without wasting excess power on heating and cooling an entire building. Because a human body has much smaller thermal mass as compared with that of an entire building, this approach should result in far higher energy efficiency (17). To achieve this

objective, it is necessary to have better control over the heat dissipation process from the human body in an indoor environment. At the normal skin temperature of 34°C, the human body emits mid-infrared (IR) radiation in the wavelength range between 7 and 14  $\mu\text{m}$ , with the peak emission at 9.5  $\mu\text{m}$  wavelength. For a typical indoor scenario, IR radiative heat dissipation contributes to more than 50% of the total body heat loss (18, 19). The objective of personal thermal management is to enhance radiative dissipation in the summer and suppress it in the winter. However, traditional textiles are not designed for infrared radiation control. We demonstrated promising results in achieving passive personal heating without energy input during cold weather by using a metallic nanowires-coated textile that reflects more than 40% of human body infrared radiation and warms up the human body (20). As for personal cooling in hot weather, we need to make textile IR-transparent in order to fully dissipate human body radiation (21). Because human skin is an excellent IR emitter (emissivity = 0.98) (22), an IR-transparent textile would allow for cooling setpoints to be higher while maintaining personal thermal comfort, with a 1° to 4°C increase in setpoint temperature translating to an energy savings of 7 to 45% (23). Unlike Peltier cooling or circulated water/air cooling, personal radiative cooling is passive and does not require integration with electronics and wiring (24, 25). The IR-transparent textile should also possess wearability properties that are comparable with traditional human cloth, such as water-wicking and air permeability.

We numerically solved the steady-state heat transfer model of clothed human skin to estimate the impact of IR-transparency of textiles on an air conditioner setpoint (Fig. 1A). The model assumes constant human skin temperature and constant metabolic generation rate, so that the air conditioner setpoint will change according to different heat transfer coefficients of the textile. The setpoint rises because of the

enhanced radiative cooling as the IR transmittance increases, approaching the limit of the bare skin case (26.6°C). Polyolefin films that have an IR-transmittance of 95% require a setpoint of 25.8°C, whereas IR-opaque materials such as cotton textile require a setpoint of 22.6°C, roughly 3°C lower.

The challenge for developing a material that is transparent to IR but opaque to visible light is that the radiation spectrum (7 to 14  $\mu\text{m}$ ) overlaps with most of the IR absorption wavelength of common textile materials—for example, C–O stretching (7.7 to 10  $\mu\text{m}$ ), C–N stretching (8.2 to 9.8  $\mu\text{m}$ ), aromatic C–H bending (7.8 to 14.5  $\mu\text{m}$ ), S=O stretching (9.4 to 9.8  $\mu\text{m}$ ), and others (26, 27). As a result, most textile materials strongly absorb human body radiation and have very low IR transparency (fig. S1). Polyolefins such as polyethylene (PE) have only aliphatic C–C and C–H bonds and consequently have narrow absorption peaks centered at the wavelengths of 3.4, 3.5, 6.8, 7.3, and 13.7  $\mu\text{m}$  (28), which are all far away from the peak of human body radiation. However, one cannot use a normal PE film as textile material because it is visibly transparent and does not have desired properties for textile, such as air permeability and water-wicking.

Here, we propose nanoporous PE (nanoPE) to be a good IR-transparent textile for human body cooling. NanoPE has interconnected pores that are 50 to 1000 nm in diameter (Fig. 1B). The pore sizes are in the size range comparable with the wavelength of visible light (400 to 700 nm), which scatter visible light strongly and make PE opaque to human eyes. The pore sizes are also much smaller than the IR wavelength, so the nanoPE film is still highly transparent to IR. The interconnected pores enable air permeability and can be water-wicking when the PE surface is chemically modified to be hydrophilic.

We modeled the visible and IR transmittance of nanoPE film using a rigorous coupled-wave analysis (RCWA) (Fig. 1C) (29). The nanoPE shows >90% total IR transmittance for wavelengths longer than 2  $\mu\text{m}$ . The nanoPE has low visible-light specular transmittance, which better represents visible appearance, owing to strong nanopore scattering (Fig. 1C). As we increased the average pore size from 200 nm to 4.8  $\mu\text{m}$ , the scattering-induced transmittance dip moved from visible to near-IR and then mid-IR (fig. S2A). All the features, including fibers and pores, are uniformly scaled, but the total thickness is fixed. The weighted-average IR transmittance based on human body radiation starts to decay at a pore size of 1.2  $\mu\text{m}$  and reaches minimum at 2.4  $\mu\text{m}$ . The transmittance dip moves to a longer wavelength at 4.8  $\mu\text{m}$ , away from the human body radiation, which slightly increases the weighted average transmittance. For thicker nanoPE, the number of nanopores along the light path increases, so the transmittance variation is more profound (fig. S2, B and C). The dimensions of fibers also influence scattering property, so we fixed the pore dimensions and investigated the fiber size effect (fig. S3). The transmittance dips occur as well, but the magnitude becomes smaller because of lower air-pore filling ratio. We

<sup>1</sup>Department of Materials Science and Engineering, Stanford University, Stanford, CA 94305, USA. <sup>2</sup>E. L. Ginzton Laboratory, Department of Electrical Engineering, Stanford University, Stanford, CA 94305, USA. <sup>3</sup>Stanford Institute for Materials and Energy Sciences, SLAC National Accelerator Laboratory, 2575 Sand Hill Road, Menlo Park, CA 94025, USA.

\*Corresponding author. Email: yicui@stanford.edu

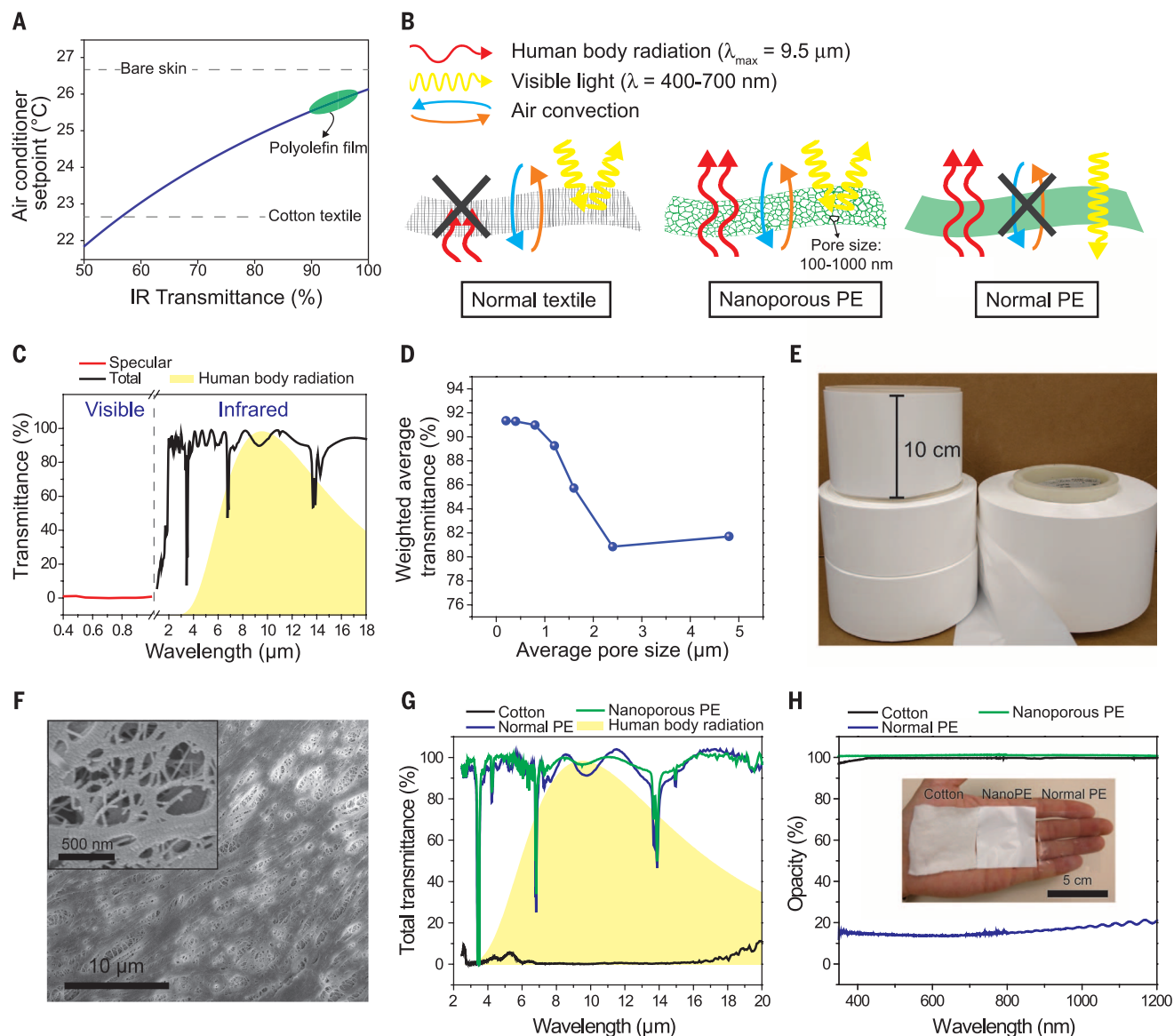


**Fig. 1. Optical property and morphology of nanoPE.** (A) Simulated air conditioner setpoint as the function of IR transmittance of textile at constant human skin temperature and metabolic generation rate. (B) Schematics of comparison between nanoPE, normal PE, and cotton. Only nanoPE satisfies IR transparency, visible light opacity, and air convection simultaneously. (C) Simulated total and specular transmittance of infrared and visible light for nanoPE, with average pore size of 400 nm. The thickness of nanoPE is 12  $\mu\text{m}$ . Human body radiation is indicated by the yellow shaded region. (D) Simulated weighted average transmittance based on human body

radiation for various pore sizes. The average transmittance drops from >90% to 80% as the pore size increases and begin to affect the transmission of human body radiation. (E) Photo of commercial nanoPE. (F) High-resolution SEM images of nanoPE. The nanopores are only 50 to 1000 nm in diameter, which is essential to ensure high IR transmittance. (G) Measured total FTIR transmittance of nanoPE, normal PE, and cotton. Because of the small pore size, nanoPE is as transparent as normal PE. Cotton, on the other hand, is completely opaque. (H) Visible opacity measurement quantitatively confirms that nanoPE is as opaque as cotton.

used the simulations as a guide for developing appropriate nanostructures for the material.

Remarkably, nanoPE is commercially available and widely used in lithium-ion batteries as a separator to prevent electrical shorting between anodes and cathodes. These PE separators (Fig. 1E) have interconnected nanopores, with ~50% pore volume for holding liquid electrolyte (30). The separators are white and have a comparable cost of ~\$2/m<sup>2</sup> to normal textiles. The commercial nanoPE has pores of 50 to 1000 nm in size and some aligned fiber-

like structure of a few micrometers wide (Fig. 1F). A zoomed-in scanning electron microscope (SEM) image (Fig. 1F, inset) clearly shows the nanopores that satisfy the size requirement of an ideal IR-transparent textile and form pathways for fluid permeation. We measured the total IR transmittance with a Fourier transform infrared (FTIR) spectrometer equipped with a diffuse gold integrating sphere (Fig. 1G). The nanopores do not affect the total IR transmittance, giving almost the same transmittance for nanoPE and normal

PE. The weighted average transmittances based on human body radiation are 96.0% for nanoPE, 93.8% for normal PE, and only 1.5% for cotton. NanoPE and cotton both exhibit white color because of visible light scattering (31), whereas normal PE is visibly transparent (Fig. 1H, inset). Quantitatively, we define opacity as (1 - specular transmittance), representing the ability to prevent objects behind the textile to be recognized. We used an ultraviolet-visible (UV-Vis) spectrometer and found that both nanoPE and cotton have

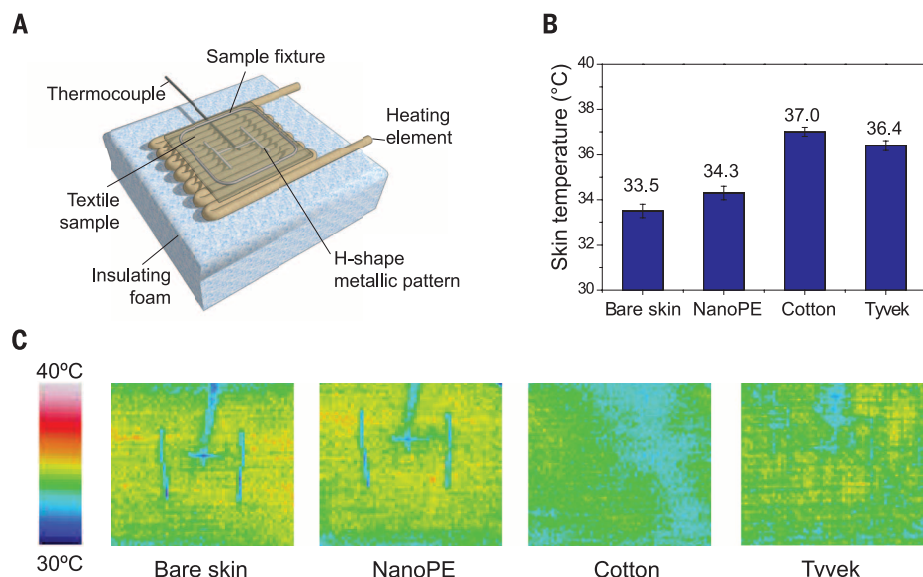


**Fig. 2. Thermal measurement of nanoPE and various textile samples.** (A) Experimental setup of textile thermal measurement. The heating element that generates constant heating power is used to simulate human skin, and the “skin temperature” is measured with the thermocouple. Lower skin temperature means a better cooling effect. (B) Thermal measurement of bare skin, nanoPE, cotton, and Tyvek. NanoPE has a much better cooling effect than that of cotton and Tyvek because of its high IR-transparency. (C) Thermal imaging of bare skin and the three samples. Only nanoPE can reveal the H-shape metallic pattern because of its IR-transparency.

opacity higher than 99% for the entire visible spectrum, whereas normal PE has only 20% opacity (Fig. 1H).

We experimentally demonstrated the cooling effect of nanoPE with a device that simulated the heat output of skin (Fig. 2A). NanoPE increases the simulated skin temperature by 0.8°C, compared with 3.5°C for cotton and 2.9°C for the fibrous PE textile Tyvek that DuPont manufactures (Fig. 2B). Because the difference between skin and ambient temperature (23.5°C) is small, this skin temperature difference can be approximated as the air conditioner setpoint difference. We used an H-shaped piece of metal to show the textile IR transmittance by use of thermal imaging (Fig. 2C). Whereas bare skin and nanoPE clearly show the H-pattern, cotton and Tyvek do not show the metallic pattern. Cotton and Tyvek also appear colder because IR radiation is blocked from transmission. Such difference in IR transmittance is because Tyvek has fiber and pore sizes that are tens of micrometers (fig. S4, A and B), which results in stronger scattering and makes it appealing for applications other than personal thermal management. At the same thickness, nanoPE is more IR-transparent than Tyvek by 9 to 14% (fig. S4C).

Besides high IR-transparency and high convective heat dissipation—which ensure superior cooling effect—wicking, mechanical strength, and

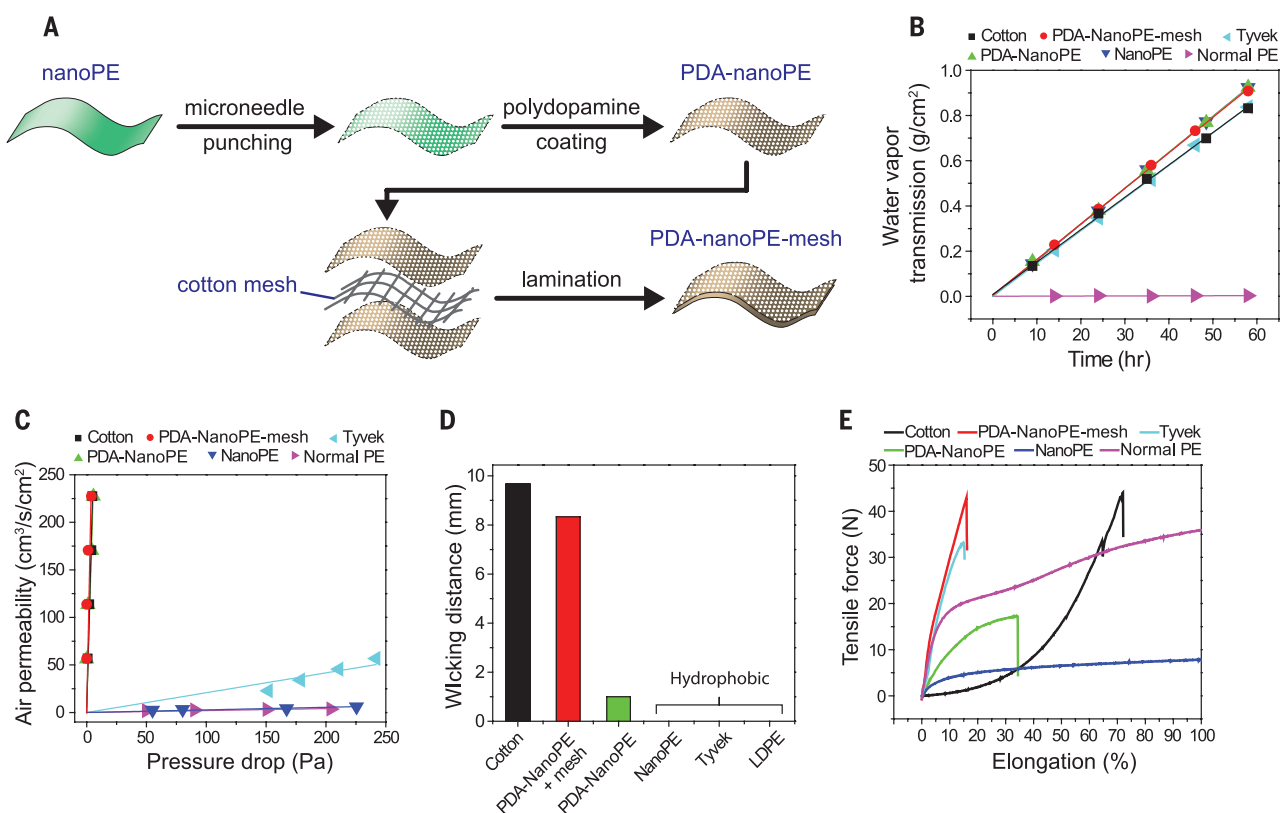


**Fig. 3. The treatment of nanoPE for various wearability testing.** (A) Schematic of the fabrication process of PDA-nanoPE-mesh. In all the textile tests, PDA-nanoPE-mesh shows performance comparable with that of cotton. (B) Water vapor transmission rate test shows how human perspiration can transmit through the textile. (C) Air permeability test examines the air flow rate through the textile at certain pressure drops. (D) Wicking distance shows the ability to transport perspiration for quick evaporation. (E) Tensile strength test demonstrates that PDA-nanoPE-mesh has the same ultimate tensile strength as that of cotton.



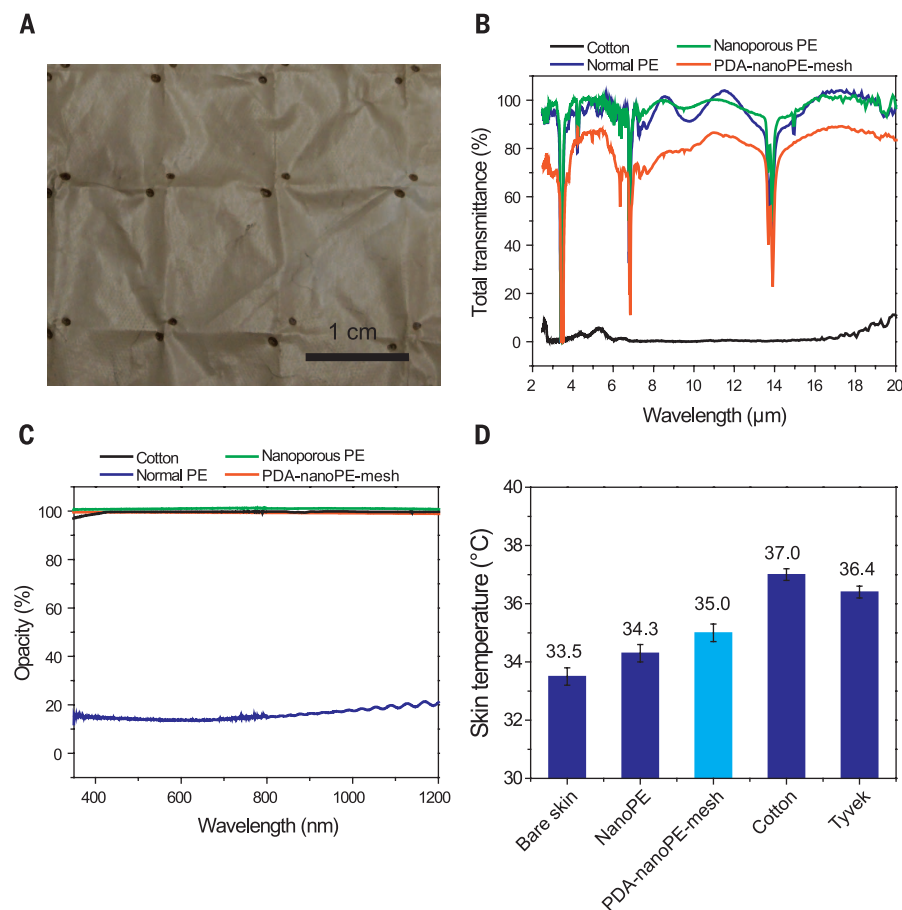


**Fig. 4. Properties of PDA-nanoPE-mesh.** (A) Photo of PDA-nanoPE-mesh. The spots that are 1 mm in diameter are the welding points. The microholes for improving air permeability are barely noticeable. (B) Total IR transmittance. (C) Visible opacity. (D) Thermal measurement.

air permeability are important for a textile to be wearable. We altered nanoPE with a number of processes in order to make it a suitable human cloth (Fig. 3A). We created 100- $\mu\text{m}$  holes spaced 500  $\mu\text{m}$  apart with commonly used microneedle punching (32). We coated the punched nanoPE with the benign hydrophilic agent polydopamine (PDA) (33–35) so as to enhance fluid wicking. We then sandwiched cotton mesh between two layers of PDA-nanoPE and bonded it with point welding in order to reinforce the mechanical strength. We performed several tests for common textile properties on PDA-nanoPE-mesh, PDA-nanoPE, nanoPE, Tyvek, cotton, and normal PE. All nanoPE samples (punched or not) have high water vapor transmission rate (WVTR) ( $\sim 0.016 \text{ g/cm}^2 \text{ hour}$ ), which is a proxy for transmitting water vapor from perspiration through natural diffusion and convection (Fig. 3B). This shows that the nanopores themselves are permeable enough for water vapor under the natural convection situation. Cotton and Tyvek have slightly lower WVTR ( $\sim 0.014 \text{ g/cm}^2 \text{ hour}$ ), and normal PE is completely nonpermeable. Air permeability is defined as the transmitted flow rate of air as a function of the applied pressure and represents the ability of the textile to let wind blow in and then carry the

body heat away. Because of the microholes that resemble the spacing between the yarns in woven cotton textile, the air permeability of PDA-nanoPE-mesh, PDA-nanoPE, and cotton are similar, in the range of 40 to 60  $\text{cm}^3/\text{s cm}^2 \text{ Pa}$  (Fig. 3C). In contrast, Tyvek, nanoPE, and normal PE show inadequate air permeability (Fig. 3C). Because the microhole size is as small as human hair (100  $\mu\text{m}$ ), the visual opaqueness is not affected. Wicking rate shows how efficiently liquid water transports in the textile. Higher wicking rate means that perspiration can spread and evaporate quickly. Cotton is well known to have a high wicking rate due to the hydrophilic cellulose fibers, with a wicking distance of 9.7 mm (Fig. 3D). PDA-nanoPE-mesh has a comparable wicking distance of 8.3 mm because of the PDA coating and capillary effect from the dual-layer structure. PDA-nanoPE is hydrophilic, but the lack of horizontal spacing limits the capillary effect. Tyvek, nanoPE, and normal PE are hydrophobic and therefore do not have any wicking length. We measured the mechanical strength of a strip of 2-cm-wide PDA-nanoPE-mesh, which can endure 45 N of tensile force (Fig. 3E). The strength is comparable with cotton and is due to the cotton mesh integrated into our fabric.

By carefully choosing the PDA thickness, microhole size, and mesh-filling ratio, PDA-nanoPE-mesh can retain good optical and thermal property (Fig. 4). The weighted average IR transmittance is 77.8%, and the opacity remains >99%. The skin temperature increases by 0.7°C compared with wearing pristine nanoPE and is 2.0°C lower than when wearing cotton textile. We demonstrated nanoPE as a favorable material to realize IR-transparent human cloth for personal thermal management. It will be worthwhile to explore the potential wearability modification methods on the basis of nanoPE. Coloration, for example, can be done by mixing with masterbatches or flexography printing. The pigments need to have a low absorption coefficient in the wavelength range of 7 to 14  $\mu\text{m}$  and be benign to the human body. Common pigments such as Prussian blue, ferric oxide, and ferrous oxide are all possible choices. PE and PDA coating are stable (36, 37), but further study such as performance evolution with perspiration, wash cycles, abrasion cycles, or ultraviolet irradiance will be meaningful for practical use.

## REFERENCES AND NOTES

- N. Oreskes, *Science* **306**, 1686 (2004).
- G. R. Walther et al., *Nature* **416**, 389–395 (2002).
- S. Chu, A. Majumdar, *Nature* **488**, 294–303 (2012).
- International Energy Agency, *World Energy Outlook Special Report on Energy and Climate Change* (International Energy Agency, 2015).
- P. Smith et al., *Nat. Clim. Change* **6**, 42–50 (2015).
- D. Kraemer et al., *Nat. Mater.* **10**, 532–538 (2011).
- N. S. Lewis et al., *Basic Research Needs for Solar Energy Utilization* (U.S. Department of Energy Office of Science, 2005).
- M. Chhowalla et al., *Nat. Chem.* **5**, 263–275 (2013).
- S. C. Roy, O. K. Varghese, M. Paulose, C. A. Grimes, *ACS Nano* **4**, 1259–1278 (2010).
- M. Molina, *The Best Value for America's Energy Dollar: A National Review of the Cost of Utility Energy Efficiency Programs* (American Council for an Energy-Efficient Economy, 2014).
- U.S. Energy Information Administration, *Annual Energy Outlook 2015 With Projections to 2040* (U.S. Energy Information Administration, 2015).
- T. Bryant et al., *Medium Term Energy Efficiency Market Report 2015* (International Energy Agency, 2015).
- A. P. Raman, M. A. Anoma, L. Zhu, E. Rephaeli, S. Fan, *Nature* **515**, 540–544 (2014).
- U.S. Department of Energy, *2011 Buildings Energy Data Book* (U.S. Department of Energy, 2012).
- International Energy Agency Energy Conservation in Buildings and Community Systems Programme, *EBC Annual Report 2014* (International Energy Agency Energy Conservation in Buildings and Community Systems Programme, 2014).
- L. Pérez-Lombard, J. Ortiz, C. Pout, *Energy Build.* **40**, 394–398 (2008).
- T. Law, *The Future of Thermal Comfort in an Energy-Constrained World*. Springer Theses (Springer International Publishing, 2013).
- J. D. Hardy, E. F. Dubois, *Proc. Natl. Acad. Sci. U.S.A.* **23**, 624–631 (1937).
- C.-E. A. Winslow, L. P. Herrington, A. P. Gagge, *Am. J. Physiol.* **127**, 505 (1939).
- P. C. Hsu et al., *Nano Lett.* **15**, 365–371 (2015).
- J. Tong et al., *ACS Photonics* **2**, 769–778 (2015).
- J. Steketee, *Phys. Med. Biol.* **18**, 686–694 (1973).
- T. Hoyt, H. L. Kwang, H. Zhang, T. E. Arens, paper presented at the International Conference on Environmental Ergonomics, Boston, 2–7 August 2009.
- D. M. Rowe, *CRC Handbook of Thermoelectrics* (CRC Press, 1995).

25. L. E. Bell, *Science* **321**, 1457–1461 (2008).
26. R. M. Silverstein, G. C. Bassler, T. C. Morrill, *Spectrometric Identification of Organic Compounds* (John Wiley and Sons, ed. 4, 1981).
27. B. H. Stuart, *Infrared Spectroscopy: Fundamentals and Applications* (John Wiley & Sons, 2005).
28. J. V. Gulmine, P. R. Janissek, H. M. Heise, L. Akcelrud, *Polym. Test.* **21**, 557–563 (2002).
29. V. Liu, S. Fan, *Comput. Phys. Commun.* **183**, 2233–2244 (2012).
30. X. Huang, *J. Solid State Electrochem.* **15**, 649–662 (2011).
31. H. L. Zhu, Z. Q. Fang, C. Preston, Y. Y. Li, L. B. Hu, *Environ. Sci.* **7**, 269–287 (2014).
32. V. Mrstina, F. Feigl, *Needle Punching: Textile Technology. Textile Science and Technology* (Elsevier, 1990).
33. H. Lee, S. M. Dellatore, W. M. Miller, P. B. Messersmith, *Science* **318**, 426–430 (2007).
34. M. H. Ryou, Y. M. Lee, J. K. Park, J. W. Choi, *Adv. Mater.* **23**, 3066–3070 (2011).
35. X. Liu et al., *ACS Nano* **7**, 9384–9395 (2013).
36. J. Jiang et al., *ACS Appl. Mater. Interfaces* **5**, 12895–12904 (2013).
37. Z.-Y. Xi, Y.-Y. Xu, L.-P. Zhu, Y. Wang, B.-K. Zhu, *J. Membr. Sci.* **327**, 244–253 (2009).

#### ACKNOWLEDGMENTS

This work was sponsored by the Advanced Research Projects Agency–Energy (ARPA-E), U.S. Department of Energy, under award DE-AR0000533. The authors thank H. Dai for lending the thermal camera. All data are available in the manuscript and the supplementary materials. Y.C., S.F., P.-C.H., A.Y.S., P.B.C., and Y.P. have a U.S. patent application (no. 62/296,549) related to this work. Y.C. and P.-C.H. conceived the idea. P.-C.H. and A.Y.S. conducted the FTIR spectrometry measurement. P.-C.H. conducted UV-Vis spectrometry measurement. P.-C.H. and C.L. designed

and conducted the thermal measurement. P.-C.H., A.Y.S., and J.X. analyzed the FTIR data. A.Y.S. performed the RCWA simulation. P.-C.H. and P.B.C. constructed and simulated heat transport model. P.-C.H. conducted SEM and optical microscope characterization. P.-C.H. and Y.P. performed wearability tests. Y.C. and S.F. supervised the project. All authors contributed to the writing of the paper.

#### SUPPLEMENTARY MATERIALS

www.sciencemag.org/content/353/6303/1019/suppl/DC1  
Materials and Methods  
Supplementary Text  
Figs. S1 to S8  
Table S1  
References (38–42)

25 February 2016; accepted 21 July 2016  
10.1126/science.aaf5471

## ASYMMETRIC CATALYSIS

# Ligand-accelerated enantioselective methylene C(sp<sup>3</sup>)-H bond activation

Gang Chen,<sup>1\*</sup> Wei Gong,<sup>1\*</sup> Zhe Zhuang,<sup>1</sup> Michal S. Andrä,<sup>1</sup> Yan-Qiao Chen,<sup>1</sup> Xin Hong,<sup>2</sup> Yun-Fang Yang,<sup>2</sup> Tao Liu,<sup>1</sup> K. N. Houk,<sup>2†</sup> Jin-Quan Yu<sup>1†</sup>

Effective differentiation of prochiral carbon–hydrogen (C–H) bonds on a single methylene carbon via asymmetric metal insertion remains a challenge. Here, we report the discovery of chiral acetyl-protected aminoethyl quinoline ligands that enable asymmetric palladium insertion into prochiral C–H bonds on a single methylene carbon center. We apply these palladium complexes to catalytic enantioselective functionalization of  $\beta$ -methylene C–H bonds in aliphatic amides. Using bidentate ligands to accelerate C–H activation of otherwise unreactive monodentate substrates is crucial for outcompeting the background reaction driven by substrate-directed cyclopalladation, thereby avoiding erosion of enantioselectivity. The potential of ligand acceleration in C–H activation is also demonstrated by enantioselective  $\beta$ -C–H arylation of simple carboxylic acids without installing directing groups.

Enantioselective functionalization of prochiral C–H bonds can potentially lead to a broad range of efficient routes to chiral compounds. Despite extensive efforts, the scope and efficiency of enantioselective C(sp<sup>3</sup>)-H activation reactions are far from adequate for broad applications in asymmetric synthesis (1, 2). Enantioselective carbene and nitrene insertions into C(sp<sup>3</sup>)-H bonds have been demonstrated in both diastereoselective and enantioselective fashion (3–7). However, asymmetric C(sp<sup>3</sup>)-H activation reactions via metal insertion are limited to the desymmetrization of two prochiral carbon centers (8–15) (Fig. 1A). For example, desymmetrizations of relatively reactive cyclopropyl and cyclobutyl C–H bonds have been achieved with Pd(II) catalysts and chiral monoprotected amino acid (MPAA) ligands (8–11). Desymmetrization of two carbon centers has also been achieved

through a Pd(0)-catalyzed intramolecular C–H arylation, as demonstrated in a series of pioneering studies (12–15). Thus far, development of an efficient chiral metal catalyst that can differentiate prochiral C–H bonds residing on a single methylene carbon center via metal insertion remains a challenge. In terms of synthetic disconnection, such a process is also distinct from the desymmetrization, as the newly created chiral center of amide substrates resides at the  $\beta$ -methylene carbon instead of the  $\alpha$ -carbon center. Recently, a transient chiral directing group has also been shown to perform enantioselective C–H arylation of benzylic C–H bonds (16). However, the transient amino acid directing group does not promote alkyl methylene C–H activation. Furthermore, the transient directing group is also incompatible with substrates derived from carboxylic acids.

The use of a bidentate 8-aminoquinoline directing group and a chiral phosphoric amide ligand has afforded moderate enantiomeric ratios (er), ranging from 74:26 to 91:9 with benzyl C–H bonds, though this method is much less successful with alkyl C–H bonds (63:37 er) (17). In general, such strongly coordinating directing groups promote ligandless C–H activation reactions, which could be detrimental for asymmetric

catalysis, as these background reactions erode enantioselectivity. Bidentate coordination from substrates also prevents the exploitation of a wide range of potentially powerful chiral bidentate ligands in palladium catalysis due to a lack of vacant coordination sites. Practically, the requirement for bidentate coordination from substrates precludes the use of a variety of simple monodentate directing groups and native functional groups to direct C–H activation, an important goal of the field.

Despite the aforementioned challenges, enantioselective  $\beta$ -C–H functionalization has long been the focus of our research efforts due to the importance of constructing  $\beta$ -chiral centers in asymmetric synthesis. Current retrosynthetic disconnections for the asymmetric synthesis of  $\beta$ -functionalized chiral carboxylic acids or amides extensively use conjugate addition reactions of the corresponding olefins. Rh(I)-catalyzed asymmetric conjugate addition of  $\alpha,\beta$ -unsaturated ketones with aryl boronic acids has afforded a useful method for the preparation of chiral  $\beta$ -arylated compounds (18, 19). However, when a given substrate or synthetic intermediate contains a saturated aliphatic acid chain without double bonds, direct enantioselective arylation of the methylene C–H bonds at the  $\beta$  position of amides through palladium insertion provides a solution (Fig. 1B). In our early efforts, we adopted a chiral auxiliary approach to gain insight into stereoselective palladium insertion into  $\beta$ -C(sp<sup>3</sup>)-H bonds (20). However, development of an enantioselective version of these diastereoselective  $\beta$ -C–H iodination and acetoxylation reactions has not been successful, owing to the lack of an appropriate ligand that can match the strongly coordinating oxazoline directing group (21). Employing a weakly coordinating amide directing group in combination with chiral MPAA ligands has led to desymmetrization of methyl, cyclopropyl, and cyclobutyl C–H bonds (Fig. 1A) at two different carbon centers (9, 10). Unfortunately, MPAA ligands have proven ineffective in promoting palladium insertion into acyclic methylene C–H bonds.

Here we report the discovery of chiral acetyl-protected aminoethyl quinoline (APAQ) ligands that enable Pd(II)-catalyzed enantioselective arylation of  $\beta$ -methylene C–H bonds of aliphatic amides, with enantiomeric ratios reaching up to 96:4 and

<sup>1</sup>The Scripps Research Institute, 10550 North Torrey Pines Road, La Jolla, CA 92037, USA. <sup>2</sup>Department of Chemistry and Biochemistry, University of California, Los Angeles, CA 90095-1569, USA.

\*These authors contributed equally to this work. †Corresponding author. Email: houk@chem.ucla.edu (K.N.H.); yu200@scripps.edu (J.-Q.Y.)

## Radiative human body cooling by nanoporous polyethylene textile

Po-Chun Hsu, Alex Y. Song, Peter B. Catrysse, Chong Liu, Yucan Peng, Jin Xie, Shanhui Fan and Yi Cui

*Science* **353** (6303), 1019-1023.  
DOI: 10.1126/science.aaf5471

### ARTICLE TOOLS

<http://science.sciencemag.org/content/353/6303/1019>

### SUPPLEMENTARY MATERIALS

<http://science.sciencemag.org/content/suppl/2016/08/31/353.6303.1019.DC1>

### RELATED CONTENT

<http://science.sciencemag.org/content/sci/353/6303/986.fullfile/content>

### REFERENCES

This article cites 26 articles, 4 of which you can access for free  
<http://science.sciencemag.org/content/353/6303/1019#BIBL>

### PERMISSIONS

<http://www.sciencemag.org/help/reprints-and-permissions>

Use of this article is subject to the [Terms of Service](#)

---

*Science* (print ISSN 0036-8075; online ISSN 1095-9203) is published by the American Association for the Advancement of Science, 1200 New York Avenue NW, Washington, DC 20005. The title *Science* is a registered trademark of AAAS.

Copyright © 2016, American Association for the Advancement of Science